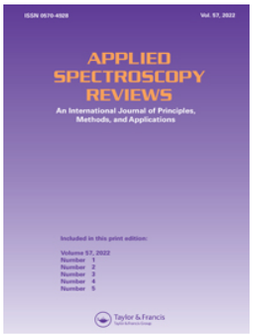

Taylor & Francis
Taylor & Francis Group

Applied Spectroscopy Reviews

ISSN: (Print) (Online) Journal homepage: https://www.tandfonline.com/loi/laps20

Application of standard and custom quartz tuning forks for quartz-enhanced photoacoustic spectroscopy gas sensing

Haoyang Lin, Yihua Liu, Leqing Lin, Wenguo Zhu, Xu Zhou, Yongchun Zhong, Marilena Giglio, Angelo Sampaolo, Pietro Patimisco, Frank K. Tittel, Jianhui Yu, Vincenzo Spagnolo & Huadan Zheng

To cite this article: Haoyang Lin, Yihua Liu, Leqing Lin, Wenguo Zhu, Xu Zhou, Yongchun Zhong, Marilena Giglio, Angelo Sampaolo, Pietro Patimisco, Frank K. Tittel, Jianhui Yu, Vincenzo Spagnolo & Huadan Zheng (2022): Application of standard and custom quartz tuning forks for quartz-enhanced photoacoustic spectroscopy gas sensing, Applied Spectroscopy Reviews, DOI: 10.1080/05704928.2022.2070917

To link to this article: https://doi.org/10.1080/05704928.2022.2070917

Published online: 15 May 2022.

APPLIED SPECTROSCOPY REVIEWS
https://doi.org/10.1080/05704928.2022.2070917

Taylor & Francis
Taylor & Francis Group

REVIEW

Application of standard and custom quartz tuning forks for quartz-enhanced photoacoustic spectroscopy gas sensing

Haoyang Lin[a], Yihua Liu[a], Leqing Lin[a], Wenguo Zhu[a], Xu Zhou[b], Yongchun Zhong[a], Marilena Giglio[c], Angelo Sampaolo[c], Pietro Patimisco[c], Frank K. Tittel[d], Jianhui Yu[a], Vincenzo Spagnolo[c], and Huadan Zheng[a]

[a]Department of Optoelectronic Engineering, Guangdong Provincial Key Laboratory of Optical Fiber Sensing and Communications, Jinan University, Guangzhou, China; [b]Craft and Hawkins Department of Petroleum Engineering, Louisiana State University, Baton Rouge, Louisiana, USA; [c]PolySense Lab—Dipartimento Interateneo di Fisica, University and Politecnico of Bari, CNR-IFN, Bari, Italy; [d]Department of Electrical and Computer Engineering, Rice University, Houston, Texas, USA

ABSTRACT

A review on the design of quartz tuning forks and their applications in quartz-enhanced photoacoustic spectroscopy (QEPAS)-based trace gas sensors is reported. Standard commercial quartz tuning forks are used as sound wave transducers in the conventional QEPAS technique. With the development of QEPAS technology, the advent of custom quartz tuning forks has further improved the sensitivity level of QEPAS sensors. The manufacturing process of quartz tuning forks will be explained in detail in this review and the application of quartz tuning forks in QEPAS trace gas sensors in recent years will be summarized.

KEYWORDS

Photoacoustic spectroscopy; gas sensor; custom quartz tuning fork

Introduction

In the 1960s, quartz tuning forks (QTFs) were widely used in clocks and watches as timing components. The vibration of the QTF is achieved by applying a small oscillating voltage to its metal electrode. The main characteristics of QTFs are: (i) the resonance frequency is determined by the prong size and the characteristics of the quartz crystal, usually in the kHz-MHz range; (ii) the frequency stability of the QTF is 0.04 ppm/T^2 frequency shift in the temperature range of –40 to 90 °C;[1] (iii) the QTF quality factor is >100,000 in the vacuum and >10,000 in the atmosphere. The frequency of a standard commercial quartz tuning fork is 32768 Hz. In 2002, Kosterev et al. exploited the piezoelectric properties of quartz in a photoacoustic gas sensing system and named this technique quartz-enhanced photoacoustic spectroscopy (QEPAS).[2] Photoacoustic spectroscopy (PAS) is an indirect absorption spectroscopy technique based on the photoacoustic effect. When the laser beam is irradiated onto the sample of the photoacoustic cell, the laser energy absorbed by the gas sample is converted into thermal energy

CONTACT Huadan Zheng zhenghuadan@jnu.edu.cn Department of Optoelectronic Engineering, Guangdong Provincial Key Laboratory of Optical Fiber Sensing and Communications, Jinan University, Guangzhou 510632, China; Vincenzo Spagnolo vincenzoluigi.spagnolo@poliba.it PolySense Lab—Dipartimento Interateneo di Fisica, University and Politecnico of Bari, CNR-IFN, Bari, Italy.

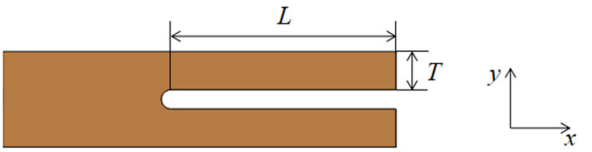

Figure 1. Floor plan of a quartz tuning fork design.

through the non-radiative relaxation process of the gas molecules, which results in local thermal expansion of the sample, causing an increase in temperature and pressure.[3] If the laser is modulated, the absorption of the laser power in the gas sample will cause the generation of sound waves. The intensity of the generated sound wave is related to the concentration of the absorbing gas sample. In photoacoustic spectroscopy, the signal amplitude S is expressed by Equations (1) and (2):[3]

$$S \sim \frac{Q \cdot P \cdot \alpha}{f} \tag{1}$$

$$\alpha = \sigma N \tag{2}$$

where Q is the quality factor of the spectrophone, P is the laser power, α is the molecular absorption coefficient, f is the laser modulation frequency, σ is the absorption cross section, and N is the target gas molecule concentration. Traditional PAS uses a sensitive microphone to detect sound waves, but its large photoacoustic unit size and low Q factor limit its performance during practical applications.[4] The QTF is used as a sharp resonance acoustic transducer in the QEPAS system to detect weak gas photoacoustic excitation.[5] The application of QTF improves the selectivity and immunity of QEPAS to environmental acoustic noise.[6] QEPAS is a robust, highly sensitive, and highly selective gas sensing spectroscopy technology with the advantages of a large dynamic range, low cost, not requiring an optical detector, allowing the use of extremely small volumes and employing an acoustic resonator that is independent of the laser wavelength. These factors, together with its proven reliability, ruggedness and compactness represent the main distinct advantages with respect to other laser-based techniques for real-world applications. Indeed, QEPAS gas sensing technology is widely used in various fields such as trace gas detection,[7,8] biomedical diagnosis,[9] chemical analysis,[10] etc.

Design of the quartz tuning fork

Theory of the quartz tuning fork

For a QTF that vibrates in a flexural mode in a plane, its prong dynamics in the direction of the rest position perpendicular to the prong can be described by the Bernoulli-Euler equation:[11]

$$\frac{\partial^4 y}{\partial x^4} + \frac{\rho \Sigma}{EI} \frac{\partial^2 y}{\partial t^2} = 0 \tag{3}$$

where $E = 0.72 \cdot 10^{11}$ N/m^2 represents Young's modulus of quartz, $\rho = 2650$ kg/m^3 represents the density of the quartz material, x is the direction determined by the prong at the rest position, and the y-direction is orthogonal to x in the QTF plane (see Figure 1).

$I(\mathrm{kg{\cdot}m^2})$ and $\Sigma(\mathrm{m^2})$ represent the moment of inertia and cross-sectional area of the prong, respectively. By applying free-clamped boundary conditions to the cantilever beam support, the above equations can be solved to determine the resonance frequency and tip shape associated with a specific time-harmonic excitation. The analytical solution of the bending vibration resonance frequency is as follows:[12]

$$f_n = \frac{\pi T}{8\sqrt{12L^2}}\sqrt{\frac{E}{\rho}}\nu_n^2 \tag{4}$$

where T is the prong width of the QTF, L is the prong length, and n is the number of mode related to each harmonic mode ($\nu_{n\,=\,0} = 1.194$ indicates the fundamental frequency mode, $\nu_{n\,=\,1} = 2.998$ indicates the first overtone mode).

Low dissipation losses of the vibrating prongs result in a sharp resonance response and a high quality factor. The Q-factor is determined by all the energy dissipation mechanisms that occur in the vibrating QTF prongs, such as losses due to surrounding fluids, support losses, surface, volume, and thermoelastic losses.[12] All these losses depend to a large extent on the size of the QTF prongs. The contribution of each loss mechanism is independent of each other, but all occur simultaneously. So far, no theoretical model can adopt a concise formula to consider all dissipation mechanisms. But by collecting a large amount of experimental data, the empirical equation related to the quality factor and the prong size is obtained, as follows:[13]

$$Q = 3.78 \times 10^5 \frac{Tw}{L} \tag{5}$$

where w represents the thickness of the quartz tuning fork.

The resistance R of the QTF represents the loss in the equivalent resonance circuit, and it determines the charge generation capacity. Through theoretical analysis, the relationship between resistance R and QTF's geometric parameters results:[14]

$$R \propto \frac{L^2}{w\sqrt{T}} \tag{6}$$

Therefore, the resonance frequency, the Q-factor, and the resistance of the QTF are strongly correlated.

Fabrication of the quartz tuning fork

The chemical composition of quartz crystal is SiO_2. The crystal is a trigonal oxide mineral, that is, low-temperature quartz (α-quartz).[15] The ideal shape of an α-quartz crystal is shown in Figure 2, with a total of 30 crystal faces. These crystal planes can be divided into five groups, with six crystal planes in each group, that is, six m-planes (or cylinders), six R-planes (or rhombohedral planes), six r-planes (or small diamond face), six s-planes and six x-planes. Each group of crystal faces has a different corrosion rate, and the slowest corrosion rate is the m-plane.[16] It can be seen from Figure 2 that the quartz crystal has a threefold axis of symmetry: the z-axis, and three secondary axes that form 120° with each other: the x_1, x_2, and x_3 axes. One of the secondary axes (such

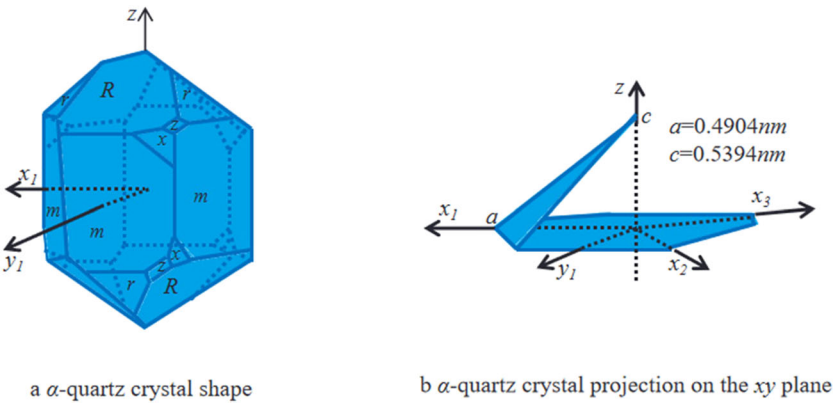

a α-quartz crystal shape

b α-quartz crystal projection on the xy plane

Figure 2. The ideal shape of an α-quartz crystal.

as the x_1 axis) can be chosen as the x-axis in the reference rectangular coordinate system, and the y-axis is perpendicular to the x and z axes.

When chemical etching is used to etch quartz, if the coordinate axis is used as the reference direction, the corrosion rate of quartz in the z-axis direction is the fastest, and the corrosion rates in the x-axis and y-axis directions are slow, basically the same. The chemical etching method is limited by the crystal tangential direction when processing quartz crystals. As a result, the chemical etching method is more suitable for processing z-cuts or cuts close to z-cuts.

The manufacturing process of a quartz tuning fork is shown in Figure 3. It can be roughly divided into the following steps: 1. Quartz double-sided plating mask; 2. Double-sided photoetching tuning fork pattern; 3. Etching of tuning fork mask; 4. Photoetching electrode pattern; 5. Chemical etching of quartz tuning fork; 6. Electrode etching; 7. Plating side electrodes.

The two sides of the quartz substrate need to be mirror polished and cleaned to remove particles, debris, organics and metal residues attached to the quartz surface. Each piece of quartz wafer is washed with a foaming cleaner in tap water and immersed in acetone for 10 minutes in an ultrasonic bath, then the quartz wafer is ultrasonically cleaned in isopropanol, and rinsed with deionized water. Each process takes ~10 minutes, the wafer can be dried with a nitrogen jet, and the cleaning process is performed in a class 1000 cleanroom environment.[17] A 600/2000 Å Cr/Au mask is deposited on the quartz wafer by thermal evaporation and magnetron sputtering to form the protective metal area of the tuning fork.[11,17] A spin coater is then used to evenly coat the photoresist on the quartz wafer. In this process, care should be taken to maintain the viscosity of the photoresist. Before exposing the quartz wafer to an ultraviolet light source, it is placed on a hot plate for soft baking to partially evaporate the solvent of the photoresist, enhancing the adhesion of the photoresist, releasing the stress in the photoresist film and preventing photoresist from contaminating the equipment. The quartz wafer is exposed to an ultraviolet light source using a standard aligner, and the transfer fork pattern is developed with a photoresist. The quartz wafer that has completed the above operation is placed on a hot plate again for baking, making the photoresist solvent continue to evaporate. The operations described above are repeated on the back of the quartz wafer. In order to protect the quartz from the etching solution of

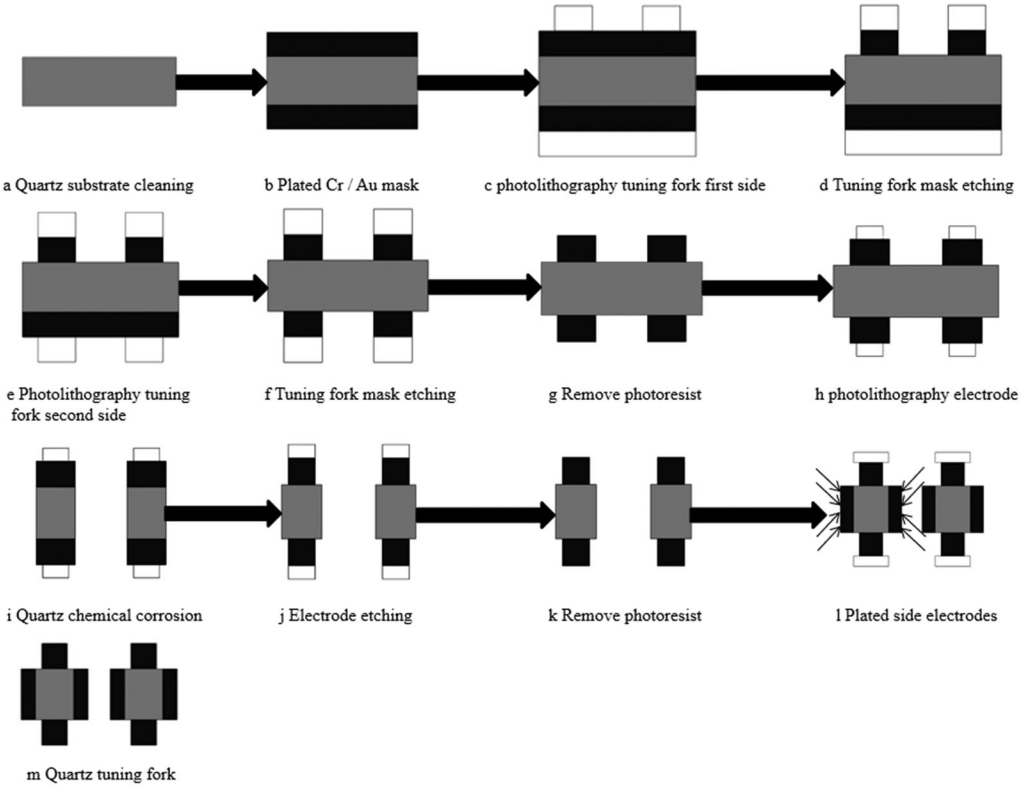

Figure 3. The fabrication process of a quartz tuning fork.

quartz, it is necessary to closely adhere to the pinhole-free metallization layer. This is achieved by stripping the photoresist pattern in acetone and relaxing the entire photoresist pattern with Cr/Au metallization areas on it.[17] As a result, photolithography and etching of the quartz tuning fork are successfully achieved. This traditional method for cutting quartz requires the use of highly toxic agents like ammonium bifluoride or HF acid. For this reason, a laser-based cutting method has been recently proposed in Ref. [18], as a clean, single pass stealth dicing process, which does not involve any chemical agent.

The shape and thickness of the electrode on the surface of the vibrating QTF prong are determined by the distribution of piezoelectric charges, which in turn depends on the stress field along the prong related to the displacement field relative to the rest position. The finite element analysis method is used to model the geometry of the quartz tuning fork, the width of the vibrating arm and the shape and thickness of the electrode on the surface of the vibrating arm to obtain the best parameters that meet the requirements. The matrix expressions for finite element analysis of elastic and piezoelectric materials are as follows:

$$\begin{bmatrix} [K_{uu}] - \omega^2[M] & [K_{u\Phi}] \\ [K_{u\Phi}]^T & [K_{\Phi\Phi}] \end{bmatrix} \begin{bmatrix} U \\ \Phi \end{bmatrix} = \begin{bmatrix} F \\ -q \end{bmatrix} \tag{7}$$

where $[K_{uu}]$ represents the stiffness matrix, $[K_{U\varphi}]$ represents the piezoelectric matrix, ω represents the angular frequency, $[M]$ represents the consistent mass matrix, $[K_{\Phi\Phi}]$

represents the dielectric matrix, U represents the vector of node values of displacement components, Φ represents the vector of node values of electric potential field and q represents the vector of the node values of the charge.[19] By solving the given matrix expression, the vibration mode, resonance frequency, stress and potential distribution, and equivalent circuit parameters can be obtained. After acquiring the electrode size parameters of the tuning fork, the electrodes of the quartz tuning fork are photolithographed. The quartz crystal is then chemically etched. The chemical anisotropic corrosion of the quartz crystal is determined by the anisotropy of the quartz crystal structure. Under the selected conditions of quartz crystal tangent, the corrosion characteristics of quartz are mainly determined by the type of corrosion solution, corrosion rate and corrosion time. Hydrofluoric acid $(HF)^+$ ammonia fluoride (NH_4F) solution can be used to corrode quartz.[20] The contour profile of the quartz tuning fork can be controlled by adjusting the concentration of hydrofluoric acid in the corrosion solution, as well as the temperature and corrosion time of the corrosion solution to remove the unwanted parts of the quartz crystal. Then it is etched through the tuning fork electrode mask to obtain the desired electrode pattern. After the above operation is completed, the quartz crystal is put into a standard photoresist stripper to strip the photoresist, and immersed in acetone, isopropyl alcohol and deionized water in order to completely remove the photoresist.[17] Finally, the side electrodes of the tuning fork are plated. When making the side electrode, the metal mask is used to cover the part of the tuning fork that does not need to be coated with Cr/Au film, and the incident direction of the membrane material molecule is adjusted to the angle of the side of the tuning fork, so that the side of the tuning fork forms a continuous and uniform film electrode.

Types of quartz tuning fork

Standard tuning fork

The principle of QEPAS is to irradiate the gas with a laser focused or collimated between the QTF prongs and modulated at a frequency matching a QTF in-plane flexural mode frequency, resulting in a transition of molecules from the ground state to the excited state. When returning to the ground state, light energy will be converted into internal energy of the molecule, causing an increase of the local temperature. Such a periodic change of the local gas pressure gives rise to a sound wave hitting the prongs of the QTF. Due to the piezoelectric effect, the tuning fork generates an electrical signal.[2]

A standard QTF, with a resonance frequency of 32.768 kHz and a Q-factor of 10,000 in the atmosphere, is a usually used transducer in QEPAS.[21] The standard QTF is made of a quartz crystal oscillator, which can be found in quartz clocks. It has been used to measure various gases, such as carbon monoxide,[22] hydrogen sulfide,[23] acetylene,[24] etc. due to its advantages of low price and stable performance. Many QEPAS spectrometers have been developed based on standard quartz tuning forks with different configurations by adding acoustic micro-resonators (AmRs). AmRs consist of one or two thin tubes positioned between or beside the QTF's prongs to amplify the acoustic vibration excited in the gas in the tube.[25] When a pair of AmRs is set close to the two sides of the QTF, and the laser beam passes through the AmRs and is focused between

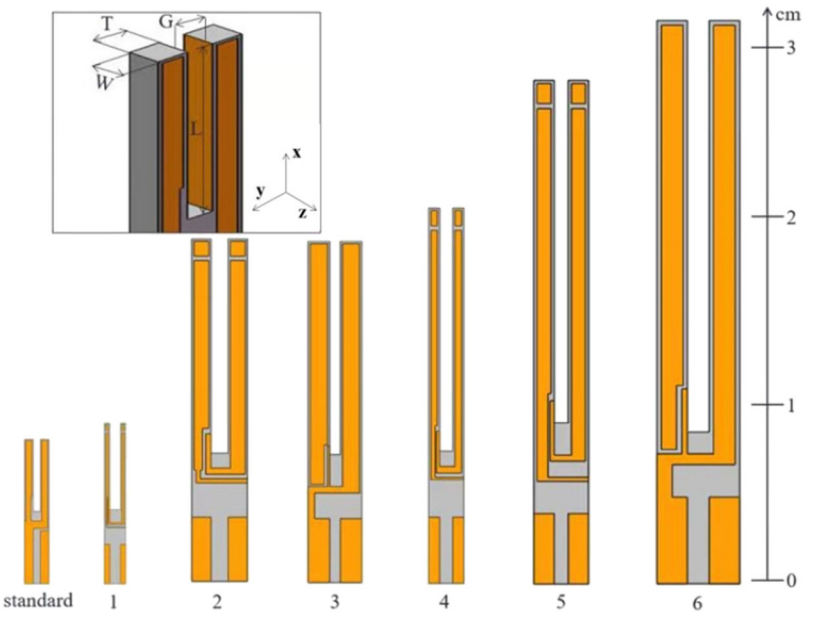

Figure 4. *x–y* plane view of standard and custom designed tuning forks presented in Ref. [28]. The size scale is shown on the right. Inset: 3D schematic view of QTF dimensions.

the QTF prongs, the configuration is called on-beam QEPAS.[26] When the laser beam passes through one AmR set behind the QTF's prongs along the *y*-axis shown in Figure 1, and a slit is opened on the AmR, in correspondence of the gap between the prongs allowing the sound wave to hit the QTF's prong, the configuration is called off-beam QEPAS. [27]

Custom tuning forks

The time constant τ for the non-radiative molecular relaxation processes typically falls in the microsecond range. The laser modulation frequency should be much lower than $1/2\pi\tau$, to allow the gas to completely convert the absorbed energy into translational energy. Therefore, the use of quartz tuning forks with resonance frequencies lower than 32 kHz would improve the gas response to the modulation of the incident laser radiation. As can be seen from Equations (1)–(3), by designing a QTF with a small width T and a large prong length L, the resonance frequency of the QTF can be reduced, but this will cause a low Q-factor and large resistance. In principle, a larger thickness w can be adopted to compensate for the Q-factor loss. However, the thickness w of the chemically etched crystal cannot be too large, otherwise the sharp edge profile cannot be guaranteed.

The first design and development of tuning forks with a different size compared with the standard tuning fork was presented in 2016. In order to clarify the effect of QTF geometric parameters on the resonance frequency f, the Q-factor and the resistance R, a series of six custom QTFs of different sizes was designed in Ref. [28]. The size of custom QTF is shown in Figure 4. Table 1 shows the dimensions and performance parameters of the tuning forks.

Table 1. Different tuning forks and their parameters;.

	f (Hz)	*Q*	*R* (Kω)	*T* (mm)	*G* (mm)	*w* (mm)	*L* (mm)
Custom QTF	14 k	7324	831.9	0.2	0.4	0.25	3.5
	7.2 k	18655	142.8	0.9	0.8	0.25	10
	8.4 k	25485	151.9	1	0.5	0.5	10
	3.4 k	8388	513.5	0.5	0.6	0.25	11
	2.8 k	11902	389.0	1	0.7	0.25	17
	4.2 k	37713	84.9	1.4	1	0.8	19
standard QTF	32.7 k	16207	79.7	0.35	0.3	0.34	3

f (resonance frequency), *Q* (Q-factor), *R* (resistance), *w* (thickness of the prong), *L* (QTF prong length), *G* (spacing between prongs), *T* (QTF prong width)

Table 2. Resonance frequency *f* and dimensions of the custom quartz tuning forks realized in recent years.

	f (Hz)	*T* (mm)	*G* (mm)	*w* (mm)	*L* (mm)	Ref.
QTF#1	4.2 k, 1st 25.4 k	1.4	0.8	0.8	17.7	[11]
QTF#2	7.2 k	0.9	0.8	0.25	10	[28]
QTF#3	20 k	\	\	\	\	[6]
QTF#4	2.8 k, 1st 17.7 k	1	0.7	0.25	17	[28]
QTF#5	3.4 k, 1st 21.5 k	0.5	0.6	0.25	11	[28]
QTF#6	1st 17.7 k	1	0.7	0.25	17	[31]
QTF#7	21.5 k	8	2	2	13.6	[32]
QTF#8	15.8 k	2	1.5	0.25	9.4	[33]
QTF#9	28 k	0.4	0.2	0.35	3.3	[34]
QTF#10	30.7 k	0.6	0.32	0.36	3.9	[35]
QTF#11*	12 k	1.4-2	0.8-1.2	0.25	9.4	[13]
QTF#12	15.2 k	2	0.8	0.25	9.4	[13]
QTF#13*	8 k	1.2-2	0.8-1.6	0.25	9.4	[36]

Notes: *f* (resonance frequency), *w* (thickness of the prong), *L* (QTF prong length), *G* (spacing between prongs), *T* (prong width), "1st": first overtone mode-frequency. "\": the parameter is not available in the reference. "-": this generation of custom QTF has multi-dimensional parameters given by the corresponding references.
*QTF#11 and QTF#13 have a T-shape geometry of the prongs.

The emergence of low-frequency custom QTFs has broken the limit of using the fundamental frequency of QTFs in QEPAS-based sensors. Thanks to the lowering of the fundamental frequency, the first overtone of the quartz tuning fork becomes available for QEPAS operations.[29] Sampaolo et al. reported that the value of the water vapor QEPAS signal to noise ratio measured for the first overtone mode of 2.8 kHz custom QTF in Table 1 is 5.3 times higher than the value obtained using fundamental mode.[30] By employing the same QTF, Wu et al. used frequency division multiplexing based on a fundamental and overtone combined QTF vibration to detect two gases at the same time, and the measured normalized noise equivalent absorption (NNEA) coefficient for H_2O and C_2H_2 were $9.12 \times 10^{-7}\,cm^{-1}$ $W/Hz^{1/2}$ and $1.51 \times 10^{-7}\,cm^{-1}$ $W/Hz^{1/2}$, respectively.[5]

Table 2 shows the resonance frequencies and dimensions of the custom QTFs (here numbered as QTF#i) demonstrated in recent years and employed in QEPAS-based sensors for trace gas detection.

QTF customization has been driven by the need for resonators vibrating at a certain frequency, with a high quality factor and low resistance, leading to a higher QEPAS signal to noise ratio, compared to the standard one. With this aim, custom QTFs have been mostly designed with the same shape as the standard QTF, but with different geometrical parameters sizes. This is the case, for example, of QTFs #1, #2 listed in Table

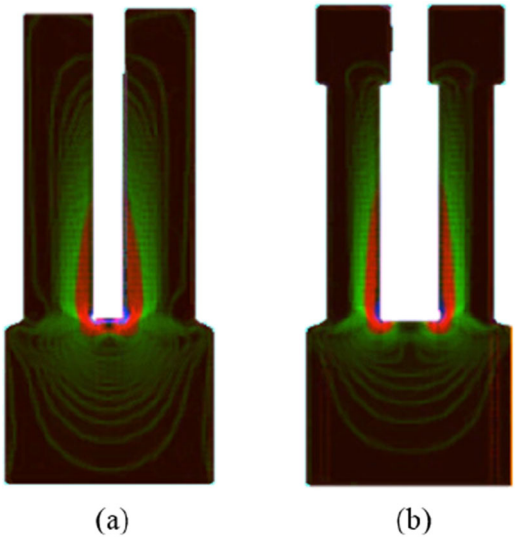

Figure 5. Stress field distribution for QTF#11 (b) and QTF#8 (a) (standard shape-like QTF having the same overall dimensions as QTF#11) simulated by COMSOL MultiPhysics®.[13]

2. However, in the last years QTFs with a different gold electrodes configuration (QTF#6) or a different shape have been developed (QTFs #11, #12).

Customized quartz tuning fork shapes have been recently developed to improve the QTF performance in terms of QEPAS signal to noise ratio. In Ref. [13], a custom T-shaped prong QTF, named QTF#11 in Table 2, exhibits improved performance thanks to an increased stress field intensity at the junction between the prong basis and the support. Figure 5 shows a comparison between the stress field distribution of the T-shaped QTF#11 and QTF#8, a standard shape-like QTF having the same overall dimensions as QTF#11, simulated by using COMSOL Multiphysics®.

The QEPAS signal of a water vapor absorption line falling at 1297.19 cm^{-1} is 1.5 times higher when employing QTF#11, compared to QTF#8. Moreover, when coupled with a pair of optimized AmRs, a signal to noise ratio enhancement of 60 is achieved, with respect to the bare QTF condition.

Another custom QTF having a shape different from the standard one is shown in Figure 6 and has been reported in Ref. [13]. This QTF is listed as QTF#12 in Table 2, reporting the resonance and geometrical parameters. In this case, rectangular grooves are carved on the front and rear surface of the prongs, reducing the resistance, thereby further increasing the signal amplitude. When targeting the same water vapor absorption line at 1297.19 cm^{-1} as for testing QTF#4, a QEPAS signal 1.36 times higher was measured, compared to QTF#8.

In 2020, on the basis of QTF#12, a new type of QTF is formed by carefully design the shape of the prong,[36] named QTF#13 in Table 2. As shown in Figure 7, after changing the ratio of T_2/T_1 from 1 to 0.6, the resonant frequency of the QTF decreased from 15.2 kHz to 8 kHz. This T-grooved QTF combined the advantages of QTF#11 and QTF#12, maintaining a Q-factor of ~11,000 in the air while maintaining a resonant frequency of <10 kHz. It was significant for the QEPAS system while detecting some gases with a slow relaxation rate, such as CO.

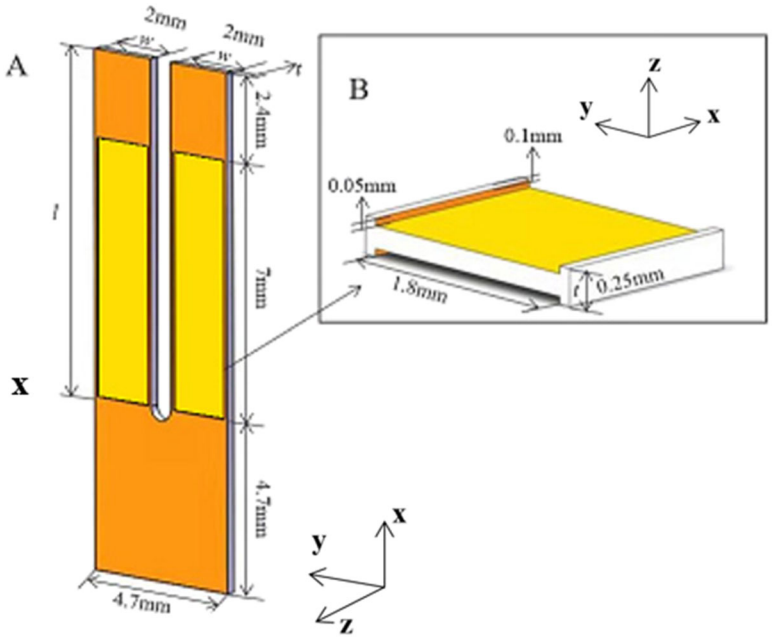

Figure 6. (A) Schematic of the geometrical dimensions of the grooved tuning fork. The yellow areas represent the carved area of the prongs surface. (B) Cross-section of grooves on the QTF.

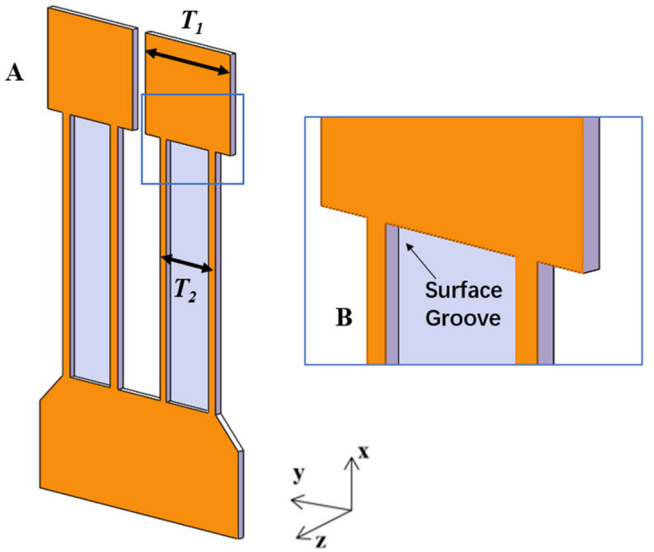

Figure 7. (A) Schematic of the T-grooved tuning fork. (B) Cross-section of grooves on the QTF.

Due to the difference between the prong displacement along the *x*-axis for the first overtone mode of the quartz tuning fork and the fundamental mode, the charge distribution on the prong surface is different.[29] A quadrupole layout is designed to match the charge distribution generated by the fundamental mode vibration. However, this quadrupole electrode configuration partially collects the piezo-charges generated when the QTF prongs vibrate at the first overtone flexural mode. Therefore, an octupole

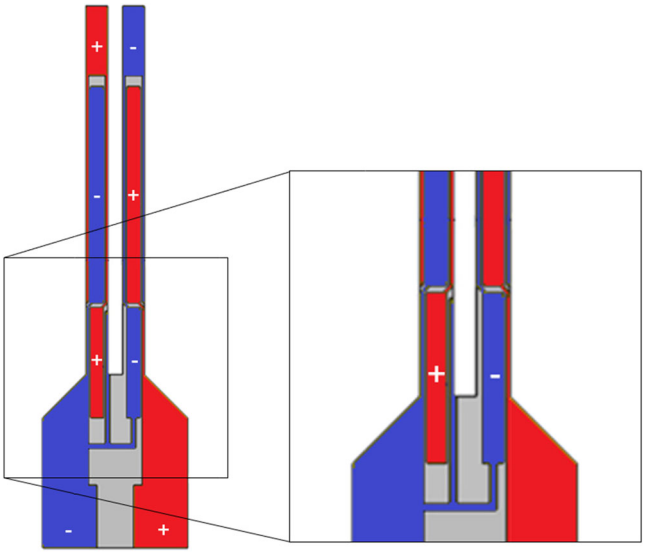

Figure 8. Schematic of the QTF#6 having an octupole electrodes pattern. A zoom of the area in which the electrode polarity is inverted is shown in the inset on the right side.

layout can be designed to improve the performance of the first overtone mode vibration.[31] Consider that an octupole pattern is not able to collect charges in case of fundamental mode vibration. Starting from the 2.8 kHz custom QTF in Table 1, having a quadrupole electrodes configuration, a QTF having the same quartz geometry but an octupole electrodes configuration has been developed. This QTF is listed as QTF#6 in Table 2 and is shown in Figure 8. The configuration of the eight-pole electrode pattern of the QTF vibrating in the first overtone mode reduces the resistance relative to the four-pole electrode pattern, and the QEPAS signal measured for a water vapor absorption line is enhanced by 2.3 times. When used in conjunction with a pair of AmRs, the QEPAS signal is further enhanced by 38 times.

Application of quartz tuning fork in QEPAS sensors

In the last decade, quartz-enhanced photoacoustic spectroscopy has been demonstrated as a gas spectroscopy technique with high specificity and high sensitivity. Numerous QEPAS sensor applications have been developed, employing the standard and custom quartz tuning forks listed in Tables 3 and 4, to detect a large number of gas species. These applications were grouped by different QTFs. For each QTF, among the QEPAS sensors targeting the same gas absorption line, only the sensor achieving the best performance in terms of noise equivalent concentration (NEC) or normalized noise equivalent absorption (NNEA) with 1 s integration time has been listed.[37]

According to Table 5, it can be known that the QEPAS system has been applied to environmental monitoring, industrial processes, agricultural production, and other application. In real-time monitoring, it showed good detection sensitivity (ppm-ppb) as well as the good specificity and long-term detection ability. However, in the QEPAS technique, the QTF needs to be in direct contact with the target gas. Since the electrode

Table 3. QEPAS detection of trace gases using standard QTF.

M	*W* (cm^{-1})	*P* (mW)	*IT* (s)	NEC (ppm)	NNEA (W cm^{-1} ▫ $Hz^{-1/2}$)	Con.	P_0 (Torr)	Ref.
H_2O	7306.75	10.2	1	0.49	1.59×10^{-7}	on-beam	200	[38]
	7194.8	5.8	1	\	1.97×10^{-8}	on-beam	760	[8]
	7181.18	\	1	2	1.2×10^{-8}	off-beam	\	[39]
CH_4	6057.09	4	\	64	\	bare QTF	298.3	[9]
	6046.95	3.74	1	4.63	1.8×10^{-8}	off-beam	760	[27]
	4348.93	2	1	0.198	\	bare QTF	223	[40]
	2988.8	\	1	0.09	\	on-beam	200	[41]
	2778.64	\	3×10^{-3}	40.75	1.3×10^{-8}	on-beam	700	[21]
	1246.46	10	1	0.011	\	bare QTF	\	[40]
CO_2	6361.25	40	247	1.74	2.2×10^{-9}	on-beam	760	[42]
	2311.1	720	20	3×10^{-4}	3.2×10^{-10}	bare QTF	37	[43]
CO	4297.7	1.8	110	13	9.3×10^{-9}	on-beam	760	[44]
	4291.5	8.8	1	11.2	1.8×10^{-5}	on-beam*	760	[45]
	2190.02	\	3×10^{-3}	0.01	2.3×10^{-8}	on-beam	700	[21]
	2103.26	80	1	0.02	2×10^{-7}	off-beam	760	[22]
NO_2	24,096.38	156	1	1.3×10^{-3}	4.2×10^{-9}	on-beam	760	[46]
NO	1900.08	133.2	0.03	4.8×10^{-3}	\	bare QTF	50	[47]
N_2O	1275.49	\	1	6×10^{-3}	\	on-beam	130	[48]
H_2S	3788.55	3	60	0.5	2.4×10^{-9}	on-beam*	124	[23]
SO_2	1380.93	48	1	0.063	1.21×10^{-8}	on-beam*	75	[49]
H_2O_2	1295.55	80	100	0.012	4.6×10^{-9}	on-beam	80	[7]
HONO	1254.85	50	150	7×10^{-3}	3.59×10^{-8}	off-beam	52	[50]
SF_6	947.93	25	1	2.75×10^{-3}	\	on-beam	75	[51]
O_2	13144.6	57	\	4	\	bare QTF	258	[9]
CS_2	2178.69	57.7	1	0.028	8.12×10^{-9}	on-beam*	56	[10]
C_2H_2	6523.88	\	\	5	\	bare QTF	760	[24]
C_2H_4	915.61	2.8	60	0.06	4.8×10^{-8}	off-beam	760	[52]
C_2H_6	2986.25	\	1	7×10^{-3}	\	on-beam	\	[41]
	2996.88	10.5	230	1.5×10^{-3}	\	on-beam	100	[53]
C_3H_8	\	\	1	3	\	on-beam	\	[41]
NH_3	965.5	48	3×10^{-3}	9.5×10^{-3}	1.42×10^{-9}	on-beam	130	[54]

Note: *M*: molecules; *W*: wavenumber of the gas absorption line; *P*: laser power between the QTF prongs; *IT*: integration time; NEC: noise equivalent concentration; NNEA: normalized noise equivalent absorption coefficient with 1 s integration time; *Con.*: QEPAS configuration; P_0: gas pressure. "*": humidify; "\": the parameter is not available in the reference. Ref. [38] was done in SF_6 carrier gas.

of QTF was made of Au/Cu, it is not suitable for detecting corrosive gases.[85] In some applications, it was necessary to detect a variety of gases. The output wavelength of the laser needs to be controlled to coincide with the absorption peak of the target gas, so several lasers need to be used in multi-gas detection, which will increase the detection cost.[86]

The development of QTF application in the last 3 years

Before 2018, in QEPAS, the first generation of custom tuning forks aimed at reducing the resonance frequencies to better detect molecules with a slow relaxation rate. Compared to a standard QTF, the prong spacing was increased to reduce photothermal background noise. In 2018, the second generation of QTF was introduced. Patimisco et al. proposed the octupole electrode pattern to better collect the electrical signal of the QTF in the fundamental frequency operating mode.[31] In 2019, the same team proposed T-shape QTF and grooved QTF to improve the QEPAS signal amplitude.[13] In 2020, T-grooved QTF with low resonance frequency (<10 kHz) and high Q-factor (~11,000) was proposed by combining T-shape QTF and grooved QTF.[36]

Table 4. QEPAS detection of trace gases using custom QTFs in Table 2.

QTF	*M*	*W* (cm^{-1})	*P* (mW)	*IT* (s)	NEC (ppm)	NNEA (W cm^{-1} ▫ $Hz^{-1/2}$)	Con.	P_0 (Torr)	Ref
#1	CH_3OH	131.05	0.04	4	7	2×10^{-10}	bare QTF	10	[11]
	CH_4	1306.1	\	10	0.2	\	on-beam†	760	[55]
	N_2O	1298	\	10	0.06	\	on-beam†	760	[56]
#2	H_2O	7306.75	\	\	\	4.5×10^{-6}	bare QTF	700	[57]
	CO_2	6361.25	37.7	1	90	1.21×10^{-8}	on-beam	760	[25]
	H_2S	6320.6	1520	1	0.89	1.29×10^{-8}	on-beam	760	[58]
	C_2H_2	6529.1	\	300	0.029	1.5×10^{-8}	bare QTF	456	[59]
#3	CH_4	3017.5	400	190	0.032	\	off-beam	760	[6]
#4	H_2O	7306.75	11.3	1	32	6.3×10^{-7}	bare QTF	200	[60]
	H_2S	97.11	0.24	30	13	4.4×10^{-10}	bare QTF	20	[61]
	CH_3OH	131.05	\	30	0.16	3.75×10^{-11}	bare QTF	10	[62]
	H_2O	7303.23	23	\	\	2.76×10^{-9}	on-beam†	760	[26]
	CH_4	3038.5	5.2	1	0.05	2.9×10^{-9}	on-beam*/†	200	[60]
		1297.47	128	0.1	0.018	\	on-beam*/†	200	[63]
	N_2O	1297.05	\	0.1	5×10^{-3}	\	on-beam*/†	200	[63]
	C_2H_2	6541.96	10	\	\	1.51×10^{-7}	bare QTF†	700	[5]
#5	C_2H_4	966.38	74.2	0.1	0.1	\	on-beam†	120	[64]
#7	CO_2	6490.05	17	1140	44	3.7×10^{-9}	on-beam	760	[32]
	C_2H_2	6490.02	17	\	\	3.9×10^{-9}	bare	760	[65]
#8	H_2S	95.62	100	10	0.36	3.1×10^{-8}	on-beam	60	[66]
	CO	2179.77	40	100	6×10^{-3}	1.6×10^{-7}	on-beam	760	[67]
#9	H_2O	7194.8	5	84	6.3	1.7×10^{-8}	bare QTF	747	[34]
	CO_2	4991.25	\	125	0.7	2×10^{-10}	on-beam	760	[68]
	C_2H_2	6507.39	5730	1	7×10^{-3}	4.4×10^{-8}	on-beam	760	[69]
#10	H_2O	7168.4	30	1	4.3	\	on-beam	760	[70]
	CO	4291.5	3.3	150	1.3	7.4×10^{-9}	on-beam*	300	[71]
	CH_4	6046.95	10	125	0.288	7.76×10^{-8}	off-beam*	760	[72]
		4290.22	6.3	100	1.2	\	on-beam	760	[73]
	C_2H_2	6534.37	1500	1	0.033	3.54×10^{-8}	on-beam	760	[74]
	NH_3	6533.4	1000	1	0.418	3.83×10^{-8}	on-beam	760	[75]
#11	$^{12}CH_4$	6046.94	12	0.1	0.76	\	on-beam	760	[76]
		3012.04	\	82	0.023	1.5×10^{-8}	on-beam	\	[77]
		2988.8	12.5	0.2	0.18	\	on-beam	200	[78]
		1296.12	\	0.1	0.6	\	on-beam	50	[41]
	$^{13}CH_4$	1296.03	\	0.1	0.11	\	on-beam	50	[41]
	CO_2	4989.97	5	270	0.45	4.7×10^{-9}	on-beam	50	[79]
	CO	2190.02	75	0.1	1.5	\	bare QTF	760	[80]
	N_2O	2190.35	75	0.1	3	\	bare QTF	760	[80]
	C_2H_4	966.38	61.6	10	0.01	\	on-beam	120	[64]
	C_2H_6	5937.3	\	0.1	22	\	on-beam	760	[81]
#12	CO	2169.2	21	0.3	7×10^{-3}	8.74×10^{-9}	on-beam*	700	[82]
	CH_4	3038.5	1.8	400	0.015	4.1×10^{-9}	on-beam*	\	[83]
	C_2H_2	6529.17	22.7	1	0.094	2.73×10^{-9}	on-beam	700	[83]
	NO_2	\	153	1	7×10^{-3}	1.54×10^{-8}	on-beam*	760	[84]
#13	CO	2169.2	20	1	0.09	1.8×10^{-7}	on-beam	500	[36]

Note: *M*: molecules; *W*: wavenumber of the gas absorption line; *P*: laser power between the QTF prongs; *IT*: integration time; NEC: noise equivalent concentration; NNEA: normalized noise equivalent absorption coefficient with 1 s integration time; *Con.*: QEPAS configuration; P_0: gas pressure. "*": humidify; "†": first overtone flexural mode; "\": the parameter is not available in the reference. Ref. [36] was done in SF_6 carrier gas.

Table 5. Real gas sensing applications based on QEPAS.

Molecules	Application	Ref
CO	Breath testing in healthy subjects of smokers.	[22]
NH_3	Diagnosis of liver and kidney diseases	[54]
CO_2	Agricultural greenhouse CO_2 detection	[68]
NO_2	Urban atmospheric NO_2 detection	[84]
CO	City road air testing	[87]
$^{12}CO_2$; $^{13}CO_2$	Helicobacter pylori infection	[88]
CH_4; C_2H_6; C_3H_8	Measuring the concentrations of the oil industry	[89]

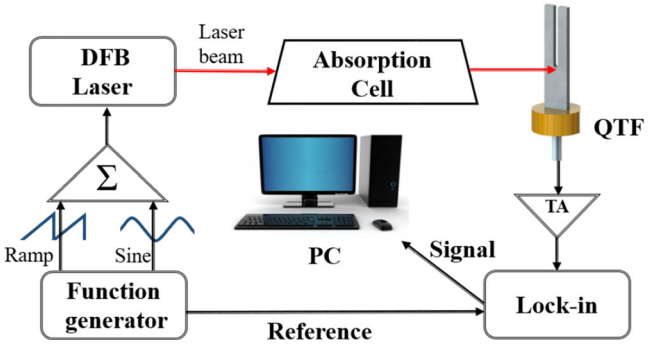

Figure 9. The configuration diagram of QEPTS.

Another progress in the last 3 years is the development of quartz-enhanced photothermal spectroscopy (QEPTS) or named light-induced thermoelastic spectroscopy (LITES) by Ma et al.[90,91] Unlike QEPAS, in QEPTS, the laser beam would focus on the QTF surface, and the piezoelectric effect induced by the thermoplastic expansion occurs. The schematic of the QEPTS was shown in Figure 9. QEPTS was a non-contact measurement method and able to remote and corrosive gas detection. Compared to QEPAS, the advantage of QEPTS is the QTF was isolated from the gas sample. This isolation will avoid the influence of contamination, humidity, and temperature changes in gases. In 2019, a multi-pass cell was added to the original QEPTS system as an absorption cell to improve the absorption length of the QEPTS sensor.[92] In 2020, a custom T-shape QTF with carved prong surfaces and a resonance frequency of ~9.35 kHz was used in QEPTS sensor, achieved a NNEA of 9.16×10^{-10} cm^{-1}W/$\sqrt{\text{Hz}}$.[93]

In 2021, Dong et al. developed a high and flat spectral responsivity photodetector based on a custom T-shape QTF.[94] The performance of the QTF detector was improved by coating absorption materials. A custom tuning fork with a fundamental resonance frequency of 9.78 kHz and quality factor of 11,500 was employed. One surface of the T-shape QTF was coated chrome/gold layer and the other was uncoated, shown in Figure 10. In a tunable diode laser absorption spectroscopy setup, five different lasers with emission wavelength in the 1.65–10.34 μm range were used to evaluate the QTF detector, achieving a responsivity of 2.2 kV/W.

Discussion

As a variant of PAS, QEPAS inherits the advantages of PAS. An important point is that the performance of QEPAS sensors improved with the increasing of laser powers according to Equation (1). This is different from other absorption spectroscopy laser techniques such as tunable diode laser absorption spectroscopy (TDLAS).[74] The signal amplitude of QEPAS is proportional to the acoustic intensity generated by the photoacoustic effect. The acoustic intensity is positively related to the laser power and the concentration of the target molecules. When the background noise and the molecular concentration remains unchanged, the higher the laser power, the greater QEPAS signal. Due to the special merits of quartz tuning fork, QEPAS were cost-effective, compact, and capable of running in real time.[63,95,96]

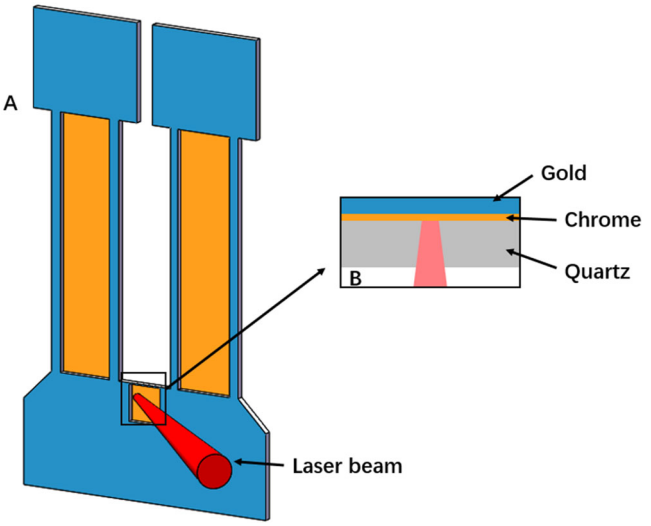

Figure 10. (A) Schematic diagram of the T-shape QTF. (B) The internal structure diagram of QTF.

As an acoustic-electric transducer, QEPAS sensor shows good environmental noise immunity, due to QTF having a high Q factor (~10,000) and narrow resonance frequency band. In addition, the QTF is a quadrupole. Sound waves from afar would push the QTF prongs to vibration in the same direction, which would not excite the piezoelectric mode of the QTF effectively.[97] Another advantage of QEPAS is the small size of QTF. In Ref. [98], a cylinder gas cell is designed to confine the PA effect induced sound waves and control the gas flow. The sampling volume was declared to be only ~0.05 mL. The gas sampling volume benefits the QEPAS sensor for fast measurement and gas analysis with small amount.

However, there are also many limitations on the QTF.[99] The resonance frequency of QTF may change with temperatures and atmospheric pressures.[100,101] With the change of temperature, the temperature field causes the changes in Young's modulus of quartz, resulting in frequency drift.[102,103] Zheng et al. reported that the resonant frequency of a standard QTF exhibits a frequency drift of 33.6 ppm from 25.6 °C to 70.4 °C.[104] In addition, with the difference of humidity, the QTF would also exhibit frequency drift caused by the change of damping effect.[105] These would be detrimental to QEPAS sensors to deal with a complex situation.

To excite the piezoelectric mode of the QTF, it was necessary to focus the laser beam between the two QTF prongs. The prong spacing for a standard QTF is ~300 μm.[8] For most case, micro-acoustic resonators in on-beam configuration was assembled with the QTF, resulting in an additional optical length of ~10 mm. The excitation light beam must be collimated through the resonator and the QTF. Any illumination on the QTF or resonator surface may result in photothermal background noise. For light sources with poor beam quality such as light emitting diodes, terahertz sources etc., this photothermal background noises are nearly unavailable.[46] Scatter light-/electrical- modulation cancelation method, or custom tuning forks with large prong spacing may solve this problem.[11,106] However, a more complex optical or electrical system will be required for the modulation cancelation method.

Conclusions

This article reviews the design and processing of quartz tuning forks, the different standard and custom types presented in literature, and their application in quartz-enhanced photoacoustic spectroscopy. We highlight the relationship between the fundamental properties of QTFs, which are resonance frequency, Q factor and equivalent resistance, and geometric parameters. We described the manufacturing process of quartz tuning fork from a piece of quartz to a complete quartz tuning fork in detail, including the cutting of crystal, the processing of electrodes, and the coupling of electrodes and crystal.

Different types of quartz tuning, including the standard tuning fork and customized tuning forks, were reported. The customization of QTFs for QEPAS applications originated from the need for: i) lower resonance frequencies to reduce the effect of molecular relaxation on the photoacoustic signal; ii) high quality factor, iii) lower electrical resistance; iv) a large gap between the prongs, to reduce the background noise due to laser light hitting the QTF; v) better piezoelectric performance and optimized charge collection; vi) optimized strain field between the prongs and their support. This led to the development of QTFs having the same shape of the standard one, but different geometrical sizes, or QTFs having different shapes compared to the standard one, i.e., T-shaped progs or carved prongs. Moreover, thanks to the low fundamental-mode resonance frequency, several QTFs were employed in QEPAS sensors exploiting the first overtone flexural mode. Such resonators also opened the way to the use of frequency division multiplexing to achieve the simultaneous detection of two gases with one tuning fork.

It is worth mentioning that silicon crystal oscillators play the role of quartz crystal competitors in certain fields, such as communication systems, time reference, etc.,[107] by virtue of their potential integration into silicon-based IC platforms. Therefore, new materials can be further employed to develop tuning forks with improved performance like for example Lithium Niobate that shows very high piezoelectric performance.[108]

Funding

This work is supported by the National Key Research and Development Program of China (2021YFB2800801, 2019YFE0118200), National Natural Science Foundation of China (12174156, 12174155, 62105125, 62005105, 62075088, 62175137), Natural Science Foundation of Guangdong Province (2020B1515020024, 2019A1515011380), the Science and Technology Projects of Guangzhou (202102020445), Key-Area Research and Development Program of Guangdong Province (2019B010138004), Project of Guangzhou Industry Leading Talents (CXLJTD-201607), Aeronautical Science Foundation of China (201808W4001), Special Project in Key Fields of the Higher Education Institutions of Guangdong Province (2020ZDZX3022), Open foundation of CEPREI (NO. 19D09), Foundation for Distinguished Young Talents in Higher Education of Guangdong (2018KQNCX009), the Fundamental Research Funds for the Central Universities (21619402, 11618413), State Key Laboratory of Applied Optics (SKLAO-201914). The authors from the Dipartimento Interateneo di Fisica di Bari acknowledge financial support from THORLABS GmbH, within the joint-research laboratory PolySense.

Disclosure statement

The authors declare no conflicts of interest.

Data availability

Data underlying the results presented in this paper are not publicly available at this time but may be obtained from the authors upon reasonable request.

References

1. Friedt, J.-M.; Carry, É. Introduction to the Quartz Tuning Fork. *Am. J. Phys* 2007, *75*, 415–422. doi:10.1119/1.2711826
2. Kosterev, A. A.; Yu, A. B.; Curl, R. F.; Tittel, F. K. Quartz-Enhanced Photoacoustic Spectroscopy. *Opt. Lett.* 2002, *27*, 1902–1904.
3. Bell, A. G. Upon the Production and Reproduction of Sound by Light. *J. Soc. Telegr. Eng.* 1880, *9*, 404–426.
4. Zheng, H.; Lou, M.; Dong, L.; Wu, H.; Ye, W.; Yin, X.; Kim, C. S.; Kim, M.; Bewley, W. W.; Merritt, C. D.; et al. Compact Photoacoustic Module for Methane Detection Incorporating Interband Cascade Light Emitting Device. *Opt. Express* 2017, *25*, 16761–16770. doi:10.1364/OE.25.016761
5. Wu, H.; Yin, X.; Dong, L.; Pei, K.; Sampaolo, A.; Patimisco, P.; Zheng, H.; Ma, W.; Zhang, L.; Yin, W.; et al. Simultaneous Dual-Gas QEPAS Detection Based on a Fundamental and Overtone Combined Vibration of Quartz Tuning Fork. *Appl. Phys. Lett.* 2017, *110*, 121104. doi:10.1063/1.4979085
6. Lassen, M.; Lamard, L.; Feng, Y.; Peremans, A.; Petersen, J. C. Off-Axis Quartz-Enhanced Photoacoustic Spectroscopy Using a Pulsed Nanosecond Mid-Infrared Optical Parametric Oscillator. *Opt. Lett.* 2016, *41*, 4118–4121. doi:10.1364/OL.41.004118
7. Ren, W.; Jiang, W.; Sanchez, N. P.; Patimisco, P.; Spagnolo, V.; Zah, C.; Xie, F.; Hughes, L. C.; Griffin, R. J.; Tittel, F. K. Hydrogen Peroxide Detection with Quartz-Enhanced Photoacoustic Spectroscopy Using a Distributed-Feedback Quantum Cascade Laser. *Appl. Phys. Lett.* 2014, *104*, 041117. doi:10.1063/1.4863955
8. Lin, H.; Huang, Z.; Kan, R.; Zheng, H.; Liu, Y.; Liu, B.; Dong, L.; Zhu, W.; Tang, J.; Yu, J.; et al. Application of Micro Quartz Tuning Fork in Trace Gas Sensing by Use of Quartz-Enhanced Photoacoustic Spectroscopy. *Sensors* 2019, *19*, 5240. doi:10.3390/s19235240
9. Milde, T.; Hoppe, M.; Tatenguem, H.; Mordmüller, M.; O'Gorman, J.; Willer, U.; Schade, W.; Sacher, J. QEPAS Sensor for Breath Analysis: A Behavior of Pressure. *Appl. Opt.* 2018, *57*, C120–C127.
10. Waclawek, J. P.; Moser, H.; Lendl, B. Compact Quantum Cascade Laser Based Quartz-Enhanced Photoacoustic Spectroscopy Sensor System for Detection of Carbon Disulfide. *Opt. Express* 2016, *24*, 6559–6571. doi:10.1364/OE.24.006559
11. Patimisco, P.; Borri, S.; Sampaolo, A.; Beere, H. E.; Ritchie, D. A.; Vitiello, M. S.; Scamarcio, G.; Spagnolo, V. A Quartz Enhanced Photo-Acoustic Gas Sensor Based on a Custom Tuning Fork and a Terahertz Quantum Cascade Laser. *Analyst* 2014, *139*, 2079–2087. doi:10.1039/c3an01219k
12. Giglio, M.; Menduni, G.; Patimisco, P.; Sampaolo, A.; Elefante, A.; Passaro, V.; Spagnolo, V. Damping Mechanisms of Piezoelectric Quartz Tuning Forks Employed in Photoacoustic Spectroscopy for Trace Gas Sensing. *Phys. Status Solidi A* 2019, *216*, 1800552. doi:10.1002/pssa.201800552
13. Patimisco, P.; Sampaolo, A.; Giglio, M.; Dello Russo, S.; Mackowiak, V.; Rossmadl, H.; Cable, A.; Tittel, F. K.; Spagnolo, V. Tuning Forks with Optimized Geometries for Quartz-Enhanced Photoacoustic Spectroscopy. *Opt. Express* 2019, *27*, 1401–1415. doi:10.1364/OE.27.001401
14. Hirata, M.; Kokubun, K.; Ono, M.; Nakayama, K. Size Effect of a Quartz Oscillator on Its Characteristics as a Friction Vacuum Gauge. *J. Vac. Sci. Technol. A* 1985, *3*, 1742–1745. doi:10.1116/1.573011

15. Hedlund, C.; Lindberg, U.; Bucht, U.; Soderkvist, J. Anisotropic Etching of Z-Cut Quartz. *J. Micromech. Microeng.* 1993, *3*, 65–73. doi:10.1088/0960-1317/3/2/006
16. Rangsten, P.; Hedlund, C.; Katardjiev, I. V.; Bäcklund, Y. Etch Rates of Crystallographic Planes in Z-Cut Quartz - Experiments and Simulation. *J. Micromech. Microeng.* 1998, *8*, 1–6. doi:10.1088/0960-1317/8/1/001
17. Lee, S.; Lee, J. Y.; Park, T. S. Fabrication of SMD 32.768 kHz Tuning Fork-Type Crystals: photolithography and Selective Etching of an Array of Quartz Tuning Fork Resonators. *Mater. Corros.* 2001, *52*, 712–715. doi:10.1002/1521-4176(200109)52:9<712::AID-MACO712>3.0.CO;2-G
18. Gaudiuso, C.; Annalisa, V.; Antonio, A. One-Step Femtosecond Laser Stealth Dicing of Quartz. *Micromachines* 2020, *11*, 327. doi:10.3390/mi11030327
19. Lee, S. Fabrication of an Array of Surface Mount Device 32.768 kHz Quartz Tuning Fork-Type Crystals: photolithography and Selective Etching of an Array of Quartz Tuning Fork Resonators with Subsequent Photoresist Spray Coating. *Vacuum* 2002, *65*, 161–168. doi:10.1016/S0042-207X(01)00477-8
20. Lee, S. Photolithography and Selective Etching of an Array of Quartz Tuning Fork Resonators with Improved Impact Resistance Characteristics. *Jpn. J. Appl. Phys.* 2001, *40*, 5164–5167. doi:10.1143/JJAP.40.5164
21. Wu, H.; Dong, L.; Zheng, H.; Yu, Y.; Ma, W.; Zhang, L.; Yin, W.; Xiao, L.; Jia, S.; Tittel, F. K. Beat Frequency Quartz-Enhanced Photoacoustic Spectroscopy for Fast and Calibration-Free Continuous Trace-Gas Monitoring. *Nat Commun.* 2017, *8*, 15331.
22. Maurin, N.; Rousseau, R.; Trzpil, W.; Aoust, G.; Hayot, M.; Mercier, J.; Bahriz, M.; Gouzi, F.; Vicet, A. First Clinical Evaluation of a Quartz Enhanced Photo-Acoustic CO Sensor for Human Breath Analysis. *Sensor. Actuat. B Chem.* 2020, *319*, 128247. doi:10.1016/j.snb.2020.128247
23. Viciani, S.; de Cumis, M. S.; Borri, S.; Patimisco, P.; Sampaolo, A.; Scamarcio, G.; De Natale, P.; D'Amato, F.; Spagnolo, V. A Quartz-Enhanced Photoacoustic Sensor for H_2S Trace-Gas Detection at 2.6 µm. *Appl. Phys. B* 2015, *119*, 21–27. doi:10.1007/s00340-014-5991-y
24. Zhang, Q.; Chang, J.; Cong, Z.; Sun, J.; Wang, Z. QEPAS Sensor for Simultaneous Measurements of H_2O, CH_4, and C_2H_2 Using Different QTFs. *IEEE Photon. J.* 2018, *10*, 1–8.
25. Zheng, H.; Dong, L.; Sampaolo, A.; Wu, H.; Patimisco, P.; Yin, X.; Ma, W.; Zhang, L.; Yin, W.; Spagnolo, V.; et al. Single-Tube on-Beam Quartz-Enhanced Photoacoustic Spectroscopy. *Opt. Lett.* 2016, *41*, 978–981.
26. Zheng, H.; Dong, L.; Sampaolo, A.; Patimisco, P.; Ma, W.; Zhang, L.; Yin, W.; Xiao, L.; Spagnolo, V.; Jia, S.; Tittel, F. K. Overtone Resonance Enhanced Single-Tube on-Beam Quartz Enhanced Photoacoustic Spectrophone. *Appl. Phys. Lett.* 2016, *109*, 111103. doi:10.1063/1.4962810
27. Hu, L.; Zheng, C.; Zhang, M.; Yao, D.; Zheng, J.; Zhang, Y.; Wang, Y.; Tittel, F. K. Quartz-Enhanced Photoacoustic Spectroscopic Methane Sensor System Using a Quartz Tuning Fork-Embedded, Double-Pass and off-Beam Configuration. *Photoacoustics* 2020, *18*, 100174. doi:10.1016/j.pacs.2020.100174
28. Patimisco, P.; Sampaolo, A.; Dong, L.; Giglio, M.; Scamarcio, G.; Tittel, F. K.; Spagnolo, V. Analysis of the Electro-Elastic Properties of Custom Quartz Tuning Forks for Optoacoustic Gas Sensing. *Sensor. Actuat. B Chem.* 2016, *227*, 539–546. doi:10.1016/j.snb.2015.12.096
29. Tittel, F. K.; Sampaolo, A.; Patimisco, P.; Dong, L.; Geras, A.; Starecki, T.; Spagnolo, V. Analysis of Overtone Flexural Modes Operation in Quartz-Enhanced Photoacoustic Spectroscopy. *Opt. Express* 2016, *24*, A682–A692. doi:10.1364/OE.24.00A682
30. Sampaolo, A.; Patimisco, P.; Dong, L.; Geras, A.; Scamarcio, G.; Starecki, T.; Tittel, F. K.; Spagnolo, V. Quartz-Enhanced Photoacoustic Spectroscopy Exploiting Tuning Fork Overtone Modes. *Appl. Phys. Lett.* 2015, *107*, 231102. doi:10.1063/1.4937002

31. Patimisco, P.; Sampaolo, A.; Giglio, M.; Mackowiak, V.; Rossmadl, H.; Gross, B.; Cable, A.; Tittel, F. K.; Spagnolo, V. Octupole Electrode Pattern for Tuning Forks Vibrating at the First Overtone Mode in Quartz-Enhanced Photoacoustic Spectroscopy. *Opt. Lett.* 2018, *43*, 1854–1857.
32. Duquesnoy, M.; Aoust, G.; Melkonian, J. M.; Lévy, R.; Raybaut, M.; Godard, A. Quartz Enhanced Photoacoustic Spectroscopy Based on a Custom Quartz Tuning Fork. *Sensors* 2019, *19*, 1362. doi:10.3390/s19061362
33. Dello Russo, S.; Giglio, M.; Sampaolo, A.; Patimisco, P.; Menduni, G.; Wu, H.; Dong, L.; Passaro, V.; Spagnolo, V. Acoustic Coupling between Resonator Tubes in Quartz-Enhanced Photoacoustic Spectrophones Employing a Large Prong Spacing Tuning Fork. *Sensors* 2019, *19*, 4109. doi:10.3390/s19194109
34. Zheng, H.; Liu, Y.; Lin, H.; Liu, B.; Gu, X.; Li, D.; Huang, B.; Wu, Y.; Dong, L.; Zhu, W.; et al. Quartz-Enhanced Photoacoustic Spectroscopy Employing Pilot Line Manufactured Custom Tuning Forks. *Photoacoustics* 2020, *17*, 100158. doi:10.1016/j.pacs.2019.100158
35. Ma, Y.; Hu, Y.; Qiao, S.; He, Y.; Tittel, F. K. Trace Gas Sensing Based on Multi-Quartz-Enhanced Photothermal Spectroscopy. *Photoacoustics* 2020, *20*, 100206. doi:10.1016/j.pacs.2020.100206
36. Sun, B.; Zifarelli, A.; Wu, H.; Dello Russo, S.; Li, S.; Patimisco, P.; Dong, L.; Spagnolo, V. Mid-Infrared Quartz-Enhanced Photoacoustic Sensor for ppb-Level CO Detection in a SF_6 Gas Matrix Exploiting a T-Grooved Quartz Tuning Fork. *Anal. Chem.* 2020, *92*, 13922–13929. doi:10.1021/acs.analchem.0c02772
37. Giglio, M.; Patimisco, P.; Sampaolo, A.; Scamarcio, G.; Tittel, F. K.; Spagnolo, V. Deviation Plot as a Tool for Quartz Enhanced Photoacoustic Sensors Noise Analysis. *IEEE Trans. Ultrason. Ferroelect. Freq. Contr.* 2016, *63*, 555–560. doi:10.1109/TUFFC.2015.2495013
38. Yin, X.; Dong, L.; Wu, H.; Gao, M.; Zhang, L.; Zhang, X.; Liu, L.; Shao, X.; Tittel, F. K. Compact QEPAS Humidity Sensor in SF_6 Buffer Gas for High-Voltage Gas Power Systems. *Photoacoustics* 2022, *25*, 100319. doi:10.1016/j.pacs.2021.100319
39. Rousseau, R.; Ayache, D.; Maurin, N.; Trzpil, W.; Bahriz, M.; Vicet, A. Monolithic Double Resonator for Quartz Enhanced Photoacoustic Spectroscopy. *Appl. Sci.* 2021, *11*, 2094. doi:10.3390/app11052094
40. Milde, T.; Hoppe, M.; Tatenguem, H.; Assmann, C.; Schade, W.; Sacher, J. Comparison of the Spectral Excitation Behavior of Methane according to InP, GaSb, IC, and QC Lasers as Excitation Source by Sensor Applications. *Appl. Opt.*. 2019, *58*, C84–C91. doi:10.1364/AO.58.000C84
41. Sampaolo, A.; Menduni, G.; Patimisco, P.; Giglio, M.; Passaro, V.; Dong, L.; Wu, H.; Tittel, F. K.; Spagnolo, V. Quartz-Enhanced Photoacoustic Spectroscopy for Hydrocarbon Trace Gas Detection and Petroleum Exploration. *Fuel* 2020, *277*, 118118. doi:10.1016/j.fuel.2020.118118
42. Zheng, H.; Dong, L.; Liu, X.; Liu, Y.; Wu, H.; Ma, W.; Zhang, L.; Yin, W.; Jia, S. Near-IR Telecommunication Diode Laser Based Double-Pass QEPAS Sensor for Atmospheric CO_2 Detection. *Laser Phys.* 2015, *25*, 125601. doi:10.1088/1054-660X/25/12/125601
43. Patimisco, P.; Borri, S.; Galli, I.; Mazzotti, D.; Giusfredi, G.; Akikusa, N.; Yamanishi, M.; Scamarcio, G.; De Natale, P.; Spagnolo, V. High Finesse Optical Cavity Coupled with a Quartz-Enhanced Photoacoustic Spectroscopic Sensor. *Analyst* 2015, *140*, 736–743. doi:10.1039/c4an01158a
44. Li, Z.; Wang, Z.; Wang, C.; Ren, W. Optical Fiber Tip-Based Quartz-Enhanced Photoacoustic Sensor for Trace Gas Detection. *Appl. Phys. B* 2016, *122*, 147. doi:10.1007/s00340-016-6435-7
45. Ma, Y.; Tong, Y.; He, Y.; Yu, X.; Tittel, F. K. High-Power DFB Diode Laser-Based CO-QEPAS Sensor: optimization and Performance. *Sensors* 2018, *18*, 122. doi:10.3390/s18010122
46. Zheng, H.; Dong, L.; Yin, X.; Liu, X.; Wu, H.; Zhang, L.; Ma, W.; Yin, W.; Jia, S. Ppb-Level QEPAS NO_2 Sensor by Use of Electrical Modulation Cancellation Method with a

High Power Blue LED. *Sensor. Actuat. B Chem.* 2015, *208*, 173–179. doi:10.1016/j.snb.2014.11.015

47. Wojtas, J.; Gluszek, A.; Hudzikowski, A.; Tittel, F. K. Mid-Infrared Trace Gas Sensor Technology Based on Intracavity Quartz-Enhanced Photoacoustic Spectroscopy. *Sensors* 2017, *17*, 513. doi:10.3390/s17030513
48. Jahjah, M.; Ren, W.; Stefański, P.; Lewicki, R.; Zhang, J.; Jiang, W.; Tarka, J.; Tittel, F. K. A Compact QCL Based Methane and Nitrous Oxide Sensor for Environmental and Medical Applications. *Analyst* 2014, *139*, 2065–2069. doi:10.1039/c3an01452e
49. Waclawek, J. P.; Lewicki, R.; Moser, H.; Brandstetter, M.; Tittel, F. K.; Lendl, B. Quartz-Enhanced Photoacoustic Spectroscopy-Based Sensor System for Sulfur Dioxide Detection Using a CW DFB-QCL. *Appl. Phys. B* 2014, *117*, 113–120. doi:10.1007/s00340-014-5809-y
50. Yi, H.; Maamary, R.; Gao, X.; Sigrist, M. W.; Fertein, E.; Chen, W. Short-Lived Species Detection of Nitrous Acid by External-Cavity Quantum Cascade Laser Based Quartz-Enhanced Photoacoustic Absorption Spectroscopy. *Appl. Phys. Lett.* 2015, *106*, 101109. doi:10.1063/1.4914896
51. Sampaolo, A.; Patimisco, P.; Giglio, M.; Chieco, L.; Scamarcio, G.; Tittel, F. K.; Spagnolo, V. Highly Sensitive Gas Leak Detector Based on a Quartz-Enhanced Photoacoustic SF_6 Sensor. *Opt. Express* 2016, *24*, 15872–15881. doi:10.1364/OE.24.015872
52. Rousseau, R.; Loghmari, Z.; Bahriz, M.; Chamassi, K.; Teissier, R.; Baranov, A. N.; Vicet, A. Off-Beam QEPAS Sensor Using an 11-μm DFB-QCL with an Optimized Acoustic Resonator. *Opt. Express* 2019, *27*, 7435–7446. doi:10.1364/OE.27.007435
53. Li, C.; Dong, L.; Zheng, C.; Lin, J.; Wang, Y.; Tittel, F. K. Ppbv-Level Ethane Detection Using Quartz-Enhanced Photoacoustic Spectroscopy with a Continuous-Wave, Room Temperature Interband Cascade Laser. *Sensors* 2018, *18*, 723. doi:10.3390/s18030723
54. Li, B.; Feng, C.; Wu, H.; Jia, S.; Dong, L. Calibration-Free Mid-Infrared Exhaled Breath Sensor Based on BF-QEPAS for Real-Time Ammonia Measurements at Ppb Level. *Sensor. Actuat. B Chem.* 2022, *358*, 131510. doi:10.1016/j.snb.2022.131510
55. Giglio, M.; Zifarelli, A.; Sampaolo, A.; Menduni, G.; Elefante, A.; Blanchard, R.; Pfluegl, C.; Witinski, M. F.; Vakhshoori, D.; Wu, H.; et al. Broadband Detection of Methane and Nitrous Oxide Using a Distributed-Feedback Quantum Cascade Laser Array and Quartz-Enhanced Photoacoustic Sensing. *Photoacoustics* 2020, *17*, 100159. doi:10.1016/j.pacs.2019.100159
56. Giglio, M.; Patimisco, P.; Sampaolo, A.; Zifarelli, A.; Blanchard, R.; Pfluegl, C.; Witinski, M. F.; Vakhshoori, D.; Tittel, F. K.; Spagnolo, V. Nitrous Oxide Quartz-Enhanced Photoacoustic Detection Employing a Broadband Distributed-Feedback Quantum Cascade Laser Array. *Appl. Phys. Lett.* 2018, *113*, 171101. doi:10.1063/1.5049872
57. Zheng, H.; Lin, H.; Dong, L.; Liu, Y.; Patimisco, P.; Zweck, J.; Mozumder, A.; Sampaolo, A.; Spagnolo, V.; Huang, B.; et al. Influence of Tuning Fork Resonance Properties on Quartz-Enhanced Photoacoustic Spectroscopy Performance. *Sensors* 2019, *19*, 3825. doi:10.3390/s19183825
58. Wu, H.; Sampaolo, A.; Dong, L.; Patimisco, P.; Liu, X.; Zheng, H.; Yin, X.; Ma, W.; Zhang, L.; Yin, W.; et al. Quartz Enhanced Photoacoustic H_2S Gas Sensor Based on a Fiber-Amplifier Source and a Custom Tuning Fork with Large Prong Spacing. *Appl. Phys. Lett.* 2015, *107*, 111104. doi:10.1063/1.4930995
59. Wang, Q.; Wang, Z.; Ren, W.; Patimisco, P.; Sampaolo, A.; Spagnolo, V. Fiber-Ring Laser Intracavity QEPAS Gas Sensor Using a 7.2 kHz Quartz Tuning Fork. *Sensor. Actuat. B Chem.* 2018, *268*, 512–518. doi:10.1016/j.snb.2018.04.139
60. Wu, H.; Dong, L.; Yin, X.; Sampaolo, A.; Patimisco, P.; Ma, W.; Zhang, L.; Yin, W.; Xiao, L.; Spagnolo, V.; Jia, S. Atmospheric CH_4 Measurement near a landfill using an ICL-based QEPAS sensor with V-T relaxation self-calibration. *Sensor. Actuat. B Chem.* 2019, *297*, 126753. doi:10.1016/j.snb.2019.126753
61. Spagnolo, V.; Patimisco, P.; Pennetta, R.; Sampaolo, A.; Scamarcio, G.; Vitiello, M. S.; Tittel, F. K. THz Quartz-Enhanced Photoacoustic Sensor for H_2S Trace Gas Detection. *Opt. Express* 2015, *23*, 7574–7582. doi:10.1364/OE.23.007574

62. Sampaolo, A.; Patimisco, P.; Giglio, M.; Vitiello, M. S.; Beere, H. E.; Ritchie, D. A.; Scamarcio, G.; Tittel, F. K.; Spagnolo, V. Improved Tuning Fork for Terahertz Quartz-Enhanced Photoacoustic Spectroscopy. *Sensors (Basel)* 2016, *16*, 439. doi:10.3390/s16040439
63. Elefante, A.; Giglio, M.; Sampaolo, A.; Menduni, G.; Patimisco, P.; Passaro, V.; Wu, H.; Rossmadl, H.; Mackowiak, V.; Cable, A.; et al. Dual-Gas Quartz-Enhanced Photoacoustic Sensor for Simultaneous Detection of Methane/Nitrous Oxide and Water Vapor. *Anal. Chem.* 2019, *91*, 12866–12873.
64. Giglio, M.; Elefante, A.; Patimisco, P.; Sampaolo, A.; Sgobba, F.; Rossmadl, H.; Mackowiak, V.; Wu, H.; Tittel, F. K.; Dong, L.; Spagnolo, V. Quartz-Enhanced Photoacoustic Sensor for Ethylene Detection Implementing Optimized Custom Tuning Fork-Based Spectrophone. *Opt. Express* 2019, *27*, 4271–4280. doi:10.1364/OE.27.004271
65. Duquesnoy, M.; Aoust, G.; Melkonian, J. M.; Levy, R.; Raybaut, M.; Godard, A. QEPAS Sensor Using a Radial Resonator. *Appl. Phys. B* 2021, *127*, 1–9. doi:10.1007/s00340-021-07699-2
66. Sampaolo, A.; Yu, C.; Wei, T.; Zifarelli, A.; Giglio, M.; Patimisco, P.; Zhu, H.; Zhu, H.; He, L.; Wu, H.; et al. H_2S Quartz-Enhanced Photoacoustic Spectroscopy Sensor Employing a Liquid-Nitrogen-Cooled THz Quantum Cascade Laser Operating in Pulsed Mode. *Photoacoustics* 2021, *21*, 100219. doi:10.1016/j.pacs.2020.100219
67. Pinto, D.; Moser, H.; Waclawek, J. P.; Russo, S. D.; Patimisco, P.; Spagnolo, V.; Lendl, B. Parts-per-Billion Detection of Carbon Monoxide: A Comparison between Quartz-Enhanced Photoacoustic and Photothermal Spectroscopy. *Photoacoustics* 2021, *22*, 100244. doi:10.1016/j.pacs.2021.100244
68. Liu, Y.; Lin, H.; Montano, B.; Zhu, W.; Zhong, Y.; Kan, R.; Yuan, B.; Yu, J.; Shao, M.; Zheng, H. Integrated near-infrared QEPAS sensor based on a 28 kHz quartz tuning fork for online monitoring of CO2 in the greenhouse . *Photoacoustics* 2022, *25*, 100332. doi:10.1016/j.pacs.2022.100332
69. Yang, Z.; Lin, H.; Montano, B.; Zhu, W.; Zhong, Y.; Yuan, B.; Yu, J.; Kan, R.; Shao, M.; Zheng, H. High-Power near-Infrared QEPAS Sensor for Ppb-Level Acetylene Detection Using a 28 kHz Quartz Tuning Fork and 10 W EDFA. *Opt. Express* 2022, *30*, 6320–6331. doi:10.1364/OE.449357
70. Ma, Y.; Yu, G.; Zhang, J.; Yu, X.; Sun, R.; Tittel, F. K. Quartz Enhanced Photoacoustic Spectroscopy Based Trace Gas Sensors Using Different Quartz Tuning Forks. *Sensors (Basel)* 2015, *15*, 7596–7604. doi:10.3390/s150407596
71. Ma, Y.; Tong, Y.; He, Y.; Jin, X.; Tittel, F. K. Compact and Sensitive Mid-Infrared All-Fiber Quartz-Enhanced Photoacoustic Spectroscopy Sensor for Carbon Monoxide Detection. *Opt. Express* 2019, *27*, 9302–9312. doi:10.1364/OE.27.009302
72. Lin, C.; Yan, X.; Huang, Y. An All-Optical off-Beam Quartz-Enhanced Photoacoustic Spectroscopy Employing Double-Pass Acoustic Microresonators. *Opt. Commun.* 2022, *503*, 127447. doi:10.1016/j.optcom.2021.127447
73. Li, Y.; Wang, R.; Tittel, F. K.; Ma, Y. Sensitive Methane Detection Based on Quartz-Enhanced Photoacoustic Spectroscopy with a High-Power Diode Laser and Wavelet Filtering. *Opt. Laser. Eng.* 2020, *132*, 106155. doi:10.1016/j.optlaseng.2020.106155
74. Ma, Y.; He, Y.; Zhang, L.; Yu, X.; Zhang, J.; Sun, R.; Tittel, F. K. Ultra-High Sensitive Acetylene Detection Using Quartz-Enhanced Photoacoustic Spectroscopy with a Fiber Amplified Diode Laser and a 30.72 kHz Quartz Tuning Fork. *Appl. Phys. Lett.* 2017, *110*, 031107. doi:10.1063/1.4974483
75. Ma, Y.; He, Y.; Tong, Y.; Yu, X.; Tittel, F. K. Ppb-Level Detection of Ammonia Based on QEPAS Using a Power Amplified Laser and a Low Resonance Frequency Quartz Tuning Fork. *Opt. Express* 2017, *25*, 29356–29364. doi:10.1364/OE.25.029356
76. Menduni, G.; Sgobba, F.; Dello Russo, S.; Ranieri, A. C.; Sampaolo, A.; Patimisco, P.; Giglio, M.; Passaro, V.; Csutak, S.; Assante, D.; et al. Fiber-Coupled Quartz Enhanced Photoacoustic Spectroscopy System for Methane and Ethane Monitoring in the near-Infrared Spectral Range. *Molecules* 2020, *25*, 5607. doi:10.3390/molecules25235607

77. Christensen, J. B.; Høgstedt, L.; Friis, S. M.; Lai, J. Y.; Chou, M. H.; Balslev-Harder, D.; Petersen, J. C.; Lassen, M. Intrinsic Spectral Resolution Limitations of QEPAS Sensors for Fast and Broad Wavelength Tuning. *Sensors* 2020, *20*, 4725. doi:10.3390/s20174725
78. Elefante, A.; Menduni, G.; Rossmadl, H.; Mackowiak, V.; Giglio, M.; Sampaolo, A.; Patimisco, P.; Passaro, V.; Spagnolo, V. Environmental Monitoring of Methane with Quartz-Enhanced Photoacoustic Spectroscopy Exploiting an Electronic Hygrometer to Compensate the H_2O Influence on the Sensor Signal. *Sensors* 2020, *20*, 2935. doi:10.3390/s20102935
79. Zhang, H.; Jin, W.; Hu, M.; Hu, M.; Liang, J.; Wang, Q. Investigation and Optimization of a Line-Locked Quartz Enhanced Spectrophone for Rapid Carbon Dioxide Measurement. *Sensors* 2021, *21*, 5225. doi:10.3390/s21155225
80. Zifarelli, A.; Giglio, M.; Menduni, G.; Sampaolo, A.; Patimisco, P.; Passaro, V.; Wu, H.; Dong, L.; Spagnolo, V. Partial Least-Squares Regression as a Tool to Retrieve Gas Concentrations in Mixtures Detected Using Quartz-Enhanced Photoacoustic Spectroscopy. *Anal. Chem.* 2020, *92*, 11035–11043.
81. Sgobba, F.; Menduni, G.; Dello Russo, S.; Sampaolo, A.; Patimisco, P.; Giglio, M.; Ranieri, E.; Passaro, V.; Tittel, F. K.; Spagnolo, V. Quartz-Enhanced Photoacoustic Detection of Ethane in the near-IR Exploiting a Highly Performant Spectrophone. *Appl. Sci.* 2020, *10*, 2447. doi:10.3390/app10072447
82. Li, S.; Dong, L.; Wu, H.; Sampaolo, A.; Patimisco, P.; Spagnolo, V.; Tittel, F. K. Ppb-Level Quartz-Enhanced Photoacoustic Detection of Carbon Monoxide Exploiting a Surface Grooved Tuning Fork. *Anal. Chem.* 2019, *91*, 5834–5840.
83. Li, S.; Wu, H.; Cui, R.; Sampaolo, A.; Patimisco, P.; Spagnolo, V.; Tittel, F. K.; Dong, L. Piezo-Enhanced Acoustic Detection Module for Mid-Infrared Trace Gas Sensing Using a Grooved Quartz Tuning Fork. *Opt. Express* 2019, *27*, 35267–35278. doi:10.1364/OE.27.035267
84. Li, S.; Lu, J.; Shang, Z.; Zeng, X.; Yuan, Y.; Wu, H.; Pan, Y.; Sampaolo, A.; Patimisco, P.; Spagnolo, V.; Dong, L. Compact Quartz-Enhanced Photoacoustic Sensor for Ppb-Level Ambient NO_2 Detection by Use of a High-Power Laser Diode and a Grooved Tuning Fork. *Photoacoustics* 2022, *25*, 100325. doi:10.1016/j.pacs.2021.100325
85. Zheng, K.; Zheng, C.; Hu, L.; Guan, G.; Ma, Y.; Song, F.; Zhang, Y.; Wang, Y.; Tittel, F. K. Light-Induced off-Axis Cavity-Enhanced Thermoelastic Spectroscopy in the near-Infrared for Trace Gas Sensing. *Opt. Express* 2021, *29*, 23213–23224. doi:10.1364/OE.430745
86. Zhang, M.; Zhong, X.; Zheng, W.; Ruan, S.; Du, B.; Yan, P.; Liang, H.; Liu, C.; Li, L.; Su, H. Widely Tunable, High Optical Signal-to-Noise Ratio Erbium-Doped Photonic Crystal Fiber Laser Suitable for Acetylene Sensing. *Opt. Laser Technol.* 2019, *109*, 525–533. doi:10.1016/j.optlastec.2018.07.035
87. Sgobba, F.; Sampaolo, A.; Patimisco, P.; Giglio, M.; Menduni, G.; Ranieri, A. C.; Hoelzl, C.; Rossmadl, H.; Brehm, C.; Mackowiak, V.; et al. Compact and Portable Quartz-Enhanced Photoacoustic Spectroscopy Sensor for Carbon Monoxide Environmental Monitoring in Urban Areas. *Photoacoustics* 2022, *25*, 100318. doi:10.1016/j.pacs.2021.100318
88. Wang, Z.; Wang, Q.; Ching, J.; Wu, J.; Zhang, G.; Ren, W. A Portable Low-Power QEPAS-Based CO_2 Isotope Sensor Using a Fiber-Coupled Interband Cascade Laser. *Sensor. Actuat. B Chem.* 2017, *246*, 710–715. doi:10.1016/j.snb.2017.02.133
89. Luo, P.; Harrist, J.; Menduni, G.; Mesdour, R.; StMichel, N.; Sampaolo, A. Simultaneous Detection of Methane, Ethane, and Propane by QEPAS Sensors for on-Site Hydrocarbon Characterization and Production Monitoring. *ACS Omega* 2022, *7*, 3395–3406. doi:10.1021/acsomega.1c05645
90. Ma, Y.; He, Y.; Tong, Y.; Yu, X.; Tittel, F. K. Quartz-Tuning-Fork Enhanced Photothermal Spectroscopy for Ultra-High Sensitive Trace Gas Detection. *Opt. Express* 2018, *26*, 32103–32110. doi:10.1364/OE.26.032103
91. Hu, L.; Zheng, C.; Zhang, Y.; Zheng, J.; Wang, Y.; Tittel, F. K. Compact All-Fiber Light-Induced Thermoelastic Spectroscopy for Gas Sensing. *Opt. Lett.* 2020, *45*, 1894–1897.

92. He, Y.; Ma, Y.; Tong, Y.; Yu, X.; Tittel, F. K. Ultra-High Sensitive Light-Induced Thermoelastic Spectroscopy Sensor with a High Q-Factor Quartz Tuning Fork and a Multipass Cell. *Opt. Lett.* 2019, *44*, 1904–1907. doi:10.1364/OL.44.001904
93. Ma, Y.; He, Y.; Patimisco, P.; Sampaolo, A.; Qiao, S.; Yu, X.; Tittel, F. K.; Spagnolo, V. Ultra-High Sensitive Trace Gas Detection Based on Light-Induced Thermoelastic Spectroscopy and a Custom Quartz Tuning Fork. *Appl. Phys. Lett.* 2020, *116*, 011103. doi:10.1063/1.5129014
94. Wei, T.; Zifarelli, A.; Dello Russo, S.; Wu, H.; Menduni, G.; Patimisco, P.; Sampaolo, A.; Spagnolo, V.; Dong, L. High and Flat Spectral Responsivity of Quartz Tuning Fork Used as Infrared Photodetector in Tunable Diode Laser Spectroscopy. *Appl. Phys. Rev.* 2021, *8*, 041409. doi:10.1063/5.0062415
95. Galli, I.; Bartalini, S.; Borri, S.; Cancio, P.; Mazzotti, D.; De Natale, P.; Giusfredi, G. Molecular Gas Sensing below Parts per Trillion: radiocarbon-Dioxide Optical Detection. *Phys. Rev. Lett.* 2011, *107*, 270802.
96. Tomberg, T.; Vainio, M.; Hieta, T.; Halonen, L. Sub-Parts-per-Trillion Level Sensitivity in Trace Gas Detection by Cantilever-Enhanced Photo-Acoustic Spectroscopy. *Sci. Rep.* 2018, *8*, 1–7.
97. Zhou, S.; Xu, L.; Zhang, L.; He, T.; Liu, N.; Liu, Y.; Yu, B.; Li, J. External Cavity Quantum Cascade Laser-Based QEPAS for Chlorodifluoromethane Spectroscopy and Sensing. *Appl. Phys. B* 2019, *125*, 1–6. doi:10.1007/s00340-019-7240-x
98. Lin, H.; Huang, Z.; Liu, Y.; Kan, R.; Zheng, H.; Zhang, R.; Zhu, W.; Tang, J.; Yu, J.; Chen, Z.; Tittel, F. K. Ultra-Compact QEPAS Acoustic Detection Module with Acoustic Wave Confinement. *Infrared Phys. Technol.* 2020, *106*, 103278. doi:10.1016/j.infrared.2020.103278
99. Chamassi, K.; Trzpil, W.; Arinero, R.; Rousseau, R.; Vicet, A.; Bahriz, M. Capacitive Silicon Micro-Electromechanical Resonator for Enhanced Photoacoustic Spectroscopy. *Appl. Phys. Lett.* 2019, *115*, 081106. doi:10.1063/1.5098140
100. Schilt, S.; Kosterev, A. A.; Tittel, F. K. Performance Evaluation of a near Infrared QEPAS Based Ethylene Sensor. *Appl. Phys. B* 2009, *95*, 813–824. doi:10.1007/s00340-008-3306-x
101. Kosterev, A. A.; Buerki, P. R.; Dong, L.; Reed, M.; Day, T.; Tittel, F. K. QEPAS Detector for Rapid Spectral Measurements. *Appl. Phys. B* 2010, *100*, 173–180. doi:10.1007/s00340-010-3975-0
102. Pielmeier, F.; Meuer, D.; Schmid, D.; Strunk, C.; Giessibl, F. J. Impact of Thermal Frequency Drift on Highest Precision Force Microscopy Using Quartz-Based Force Sensors at Low Temperatures. *Beilstein J. Nanotechnol.* 2014, *5*, 407–412. doi:10.3762/bjnano.5.48
103. Brendel, R. Influence of a Magnetic Field on Quartz Crystal Resonators. *IEEE Trans. Ultrason. Ferroelect. Freq. Contr.* 1996, *43*, 818–831. doi:10.1109/58.535482
104. Zhang, Y.; Lv, H.; Zheng, H.; Liu, Y.; Lin, H.; Zhu, W.; Yu, J.; Chen, Z.; Tittel, F. K. Temperature-Compensated Calibration for Quartz-Enhanced Photoacoustic Spectroscopy by Thermoelastic Effects. *Infrared Phys. Technol.* 2021, *117*, 103816. doi:10.1016/j.infrared.2021.103816
105. Ko, J.; Yoon, Y.; Lee, J. Quartz Tuning Forks with Hydrogel Patterned by Dynamic Mask Lithography for Humidity Sensing. *Sensor. Actuat. B: Chem.* 2018, *273*, 821–825. doi:10.1016/j.snb.2018.06.099
106. Zheng, H.; Dong, L.; Ma, Y.; Wu, H.; Liu, X.; Yin, X.; Zhang, L.; Ma, W.; Yin, W.; Xiao, L.; Jia, S. Scattered Light Modulation Cancellation Method for Sub-Ppb-Level NO_2 Detection in a LD-Excited QEPAS System. *Opt. Express* 2016, *24*, A752–A761. doi:10.1364/OE.24.00A752
107. Muller, C.; Baborowski, J.; Pezous, A.; Dubois, M.-A. Experimental Evidence of Thermoelastic Damping in Silicon Tuning Fork. *Proc. Chem.* 2009, *1*, 1395–1398. doi:10.1016/j.proche.2009.07.348
108. Warner, A. W.; Onoe, M.; Coquin, G. A. Determination of Elastic and Piezoelectric Constants for Crystals in Class (3m). *J. Acoust. Soc. Am.* 1967, *42*, 1223–1231. [Database] doi:10.1121/1.1910709